Revealing the nanogeometry of WS2 nanoflowersby polarization-resolved Raman spectroscopy

Komen, I.; van Heijst, S.E.; Caldarola, M.; Conesa Boj, S.; Kuipers, L.

DOI
10.1063/5.0102381

Publication date
2022

Document Version
Final published version

Published in
Journal of Applied Physics

Journal of Applied Physics

Revealing the nanogeometry of WS_2 nanoflowers by polarization-resolved Raman spectroscopy

Cite as: J. Appl. Phys. **132**, 173103 (2022); https://doi.org/10.1063/5.0102381
Submitted: 09 June 2022 • Accepted: 16 September 2022 • Published Online: 01 November 2022

Irina Komen, Sabrya E. van Heijst, Martin Caldarola, et al.

Journal of Applied Physics ARTICLE scitation.org/journal/jap

Revealing the nanogeometry of WS_2 nanoflowers by polarization-resolved Raman spectroscopy

Cite as: J. Appl. Phys. **132**, 173103 (2022); doi: 10.1063/5.0102381
Submitted: 9 June 2022 · Accepted: 16 September 2022 ·
Published Online: 1 November 2022

Irina Komen, Sabrya E. van Heijst, Martin Caldarola, Sonia Conesa-Boj, and L. Kuipers[a)]

AFFILIATIONS

Quantum Nanoscience, Kavli Institute of Nanoscience, Delft University of Technology, Delft, The Netherlands

[a)]**Author to whom correspondence should be addressed** L.Kuipers@tudelft.nl

ABSTRACT

Recent studies of transition metal dichalcogenides (TMDs) have revealed exciting optical properties, such as stable excitons and chiral light–matter interactions. Chemical vapor deposition techniques provide a platform for the fabrication of nanostructures with diverse geometries, ranging from horizontal flakes to flower-like structures. Raman spectroscopy is commonly used to characterize TMDs and their properties. Here, we use polarization-resolved Raman spectroscopy to probe the nanogeometry and orientation of WS_2 nanoflower petals. Exciting the nanoflowers with linearly polarized light, we observe an enhanced Raman response from flower petals oriented along the excitation polarization direction. Furthermore, the helicity-resolved Raman response of vertically oriented wall-like flower petals exhibits clear differences with horizontally oriented flakes. Although the photoluminescence from the nanoflowers is strongly reduced, the Raman response upon excitation in resonance with the WS_2 excitonic transition does reveal the presence of the exciton, which results in a distinct temperature dependence of the Raman response.

I. INTRODUCTION

Recently, great scientific interest has been taken in transition metal dichalcogenides (TMDs) and their fascinating optical properties.[1] TMD materials, such as MoS_2, WS_2, $MoSe_2$, and WSe_2, being semiconductors with a bandgap in the visible wavelength range, offer many possibilities for applications in opto-electronics.[2,3] In the TMD semiconductor valleys, electron and hole pairs form stable excitons even at room temperature.[4] Moreover, the interaction of TMDs with light is chiral, as their pseudospin allows selective addressing of each TMD valley by circularly polarized light with opposite handedness.[5–7]

Chemical vapor deposition (CVD) provides a flexible platform for the fabrication of TMD nanostructures.[8–13] While CVD can reproduce naturally occurring flat-layered TMDs, it also offers the possibility of fabricating vertical TMD walls,[14] pyramids,[15] and flower-like nanostructures.[16–19] Due to a large amount of edges and chemically active sites, flower-like TMD structures are investigated for applications ranging from catalysis[18,19] to using their large field emission as a potential electron source.[16,17] However, so far, TMD nanoflowers have mainly been studied using electron microscopy tools,[19] and little is known about their interaction with light. It is interesting to note that in contrast to flat layers, no photoluminescence (PL) but only a Raman response is reported from vertical TMD walls,[14,20] TMD pyramids,[15] or flower-like TMD structures.[16–18]

Raman spectroscopy offers a powerful, fast, and non-invasive tool for the investigation of TMD materials.[21–24] Commonly studied in TMDs are the characteristic vibrational modes, namely, E^1_{2g}, which corresponds to the in-plane displacement of the atoms, and A_{1g}, which corresponds to the out-of-plane displacement of the chalcogenide atoms, as well as the longitudinal acoustic phonon LA(M). Interestingly, the TMD Raman response is highly enhanced when the excitation is on resonance with an excitonic transition.[23,25–27] As this resonance effect can be observed in the Raman response even in the absence of photoluminescence, resonance Raman spectroscopy offers a way to study the TMD exciton indirectly.[15] Since the TMD bandgap energy depends on temperature, varying the temperature of a TMD material enables the tuning of the resonance condition for a fixed excitation frequency. Therefore, studying TMDs at various cryogenic temperatures provides insights on the influence of the excitonic transition on the Raman response. Moreover, temperature-dependent Raman spectroscopy can shed light on the structural properties of TMD materials.[28,29]

The Raman response of TMDs is influenced by the polarization of the excitation light, where the in-plane and out-of-plane

vibrations of the atoms respond differently to either orthogonal or in-plane polarization.[22] Furthermore, given the chirality of the TMD valleys and the resonant influence of the excitons on the Raman response, studying the interaction of TMD phonons with circularly polarized light is important.[30–32] As the Raman effect depends on the polarizability of the material, the interaction of TMDs with polarized light is described by a Raman polarizability tensor.[31,33,34] It is important to note that these tensors are defined with respect to the atomic axes, e.g., typically assuming flat-layered TMDs with the excitation light perpendicular to it. Thus, the polarization-resolved Raman response of, for instance, a vertical TMDs wall will be completely different from that of a flat layer; e.g., modes that are usually allowed/forbidden in cross-polarization will now be absent/observed.[20,33–35] Therefore, polarization-resolved Raman studies will provide insight into the flowers' nano-geometry and orientation in the 3D space, e.g., its orientation with respect to the substrate.

In this work, we study the polarization- and temperature-dependent optical response of WS_2 nanoflowers. The nanoflowers exhibit a highly reduced PL enabling the study of, therefore, the unobscured Raman response. At first glance, no spectral differences are observed between WS_2 flowers of different geometry except for differences in Raman intensity. However, polarization- and helicity-resolved Raman spectroscopy reveals underlying structural differences between flowers. We find that petals of the flowers oriented vertically exhibit a different response to circularly polarized light than more flat flower petals. Moreover, we find that the relative in-plane orientation of the flower petals with respect to the polarization direction of linearly polarized light affects the optical response. Surprisingly, the polarization- and helicity-dependent behavior of the characteristic in-plane and out-of-plane WS_2 Raman modes is similar, indicating the similarity of the underlying Raman tensors. Studying the temperature-dependent spectral response of WS_2 nanoflowers, we observe the influence of the excitonic resonance on the Raman intensity, helicity, and the ratio between the two characteristic WS_2 Raman features.

II. RESULTS AND DISCUSSION

A. Optical response of WS_2 nanoflowers

Figure 1(a) depicts a scanning electron microscopy (SEM) image of the flower-like WS_2 nanostructures (nanoflowers) studied in this work. In the same way as natural flowers, these WS_2 nanostructures consist of randomly oriented flakes (the petals) expanding from a common point. The nanostructures are fabricated using CVD on an Si_3N_4 membrane (200 nm thickness) with an array of holes

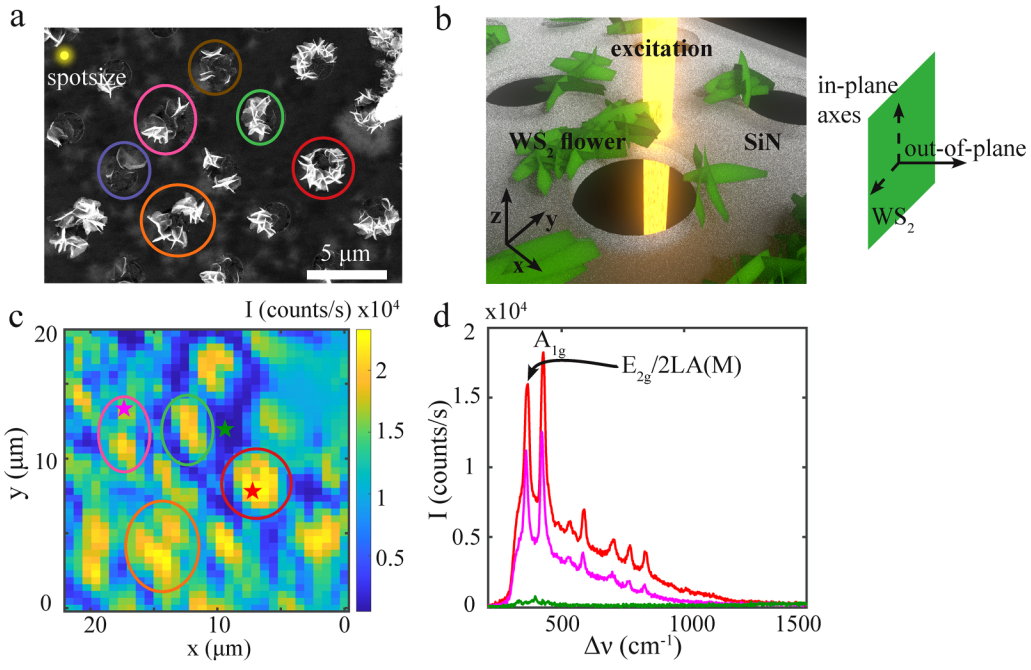

FIG. 1. Optical response of WS_2 nanoflowers. (a) SEM image of the WS_2 nanoflowers on an SiN membrane with circular holes. The flowers grow mainly around the holes, forming diverse flower-like shapes ranging from circles (red) and half-circles (green) to vertical walls (brown, pink) and more chaotic structures (orange, pink, lilac). The size of the excitation laser spot (500 nm) is in yellow. (b) A schematic representation of the SiN substrate (gray) with holes (black), WS_2 nanoflowers (green), and the excitation laser (yellow). (side panel) A schematic representation of one WS_2 nanoflower petal with its crystallographic axes. While the out-of-plane crystallographic axis is always oriented perpendicular to the flake, the in-plane crystal axes lie in the plane of the flake with an unknown azimuthal angle. (c) Map of the peak intensity of the first Raman feature [denoted with an arrow in (d)], where the shape of the flowers can be clearly correlated with the SEM image in (a) (see colored circles as a guide to the eye). (d) Spectra at different positions indicated with stars in (c) on flowers (red and pink) and on the substrate (green). Note that, even though the flowers have a diversity in shapes, the only difference between spectra of flowers is the intensity of the Raman features.

[2 μm radius and 4 μm pitch, see Fig. S3(a) in the supplementary material]. A description of the fabrication of the WS_2 nanoflowers, together with an extensive characterization of their electronic and crystallographic properties, is presented in Van Heijst *et al.*[19] We emphasize that the crystallographic analysis of Ref. 19 is performed exactly on the same sample as the one studied optically here, with the advantage that optical characterization is relatively fast with respect to electron microscopy, and can be performed on larger and even wafer-scale areas. The WS_2 nanoflowers arise mainly around the holes in the substrate [see Fig. 1(a)], forming diverse shapes ranging from circles (red) and half-circles (green) to vertical walls (brown, pink) and more complex structures (orange, pink, lilac). The larger structure to the right of Fig. 1(a) is probably a conglomeration of WS_2 grown around a dust particle. Figure 1(b) schematically presents the nanoflowers (green) around the holes (black) in the substrate (gray). The excitation light is along the z axis, and the orientation of the flower petals ranges from completely flat (in the x–y plane) to standing up (the x–z or y–z plane). The nanoflower petals are composed of multiple terraces with different thicknesses, varying between 2 and 30 nm.[19] The high-resolution scanning transmission electron microscopy (HRSTEM) study in Ref. 19 reveals that the nanoflowers exhibit a crystallographic 2H/3R polytypism (see Sec. II B in the supplementary material for details). While the out-of-plane crystallographic axis is always oriented perpendicular to the flake, the in-plane crystal axes lie in the plane of the flake with an unknown azimuthal angle [see the side panel of Fig. 1(b)]. The basal plane is common for all of the analyzed WS_2 nanostructures, and it is given by the (0001) direction.[19]

We investigate the optical response of the WS_2 nanoflowers, which consists mainly of a Raman response. Figure 1(c) presents the intensity of the first Raman feature [see the arrow in Fig. 1(d)] of the flowers depicted in Fig. 1(a). The Raman map can be correlated with the SEM image by comparing the shape and relative position of the flowers [e.g., compare the colored circles in Figs. 1(a) and 1(c)]. Not surprisingly, the more dense flowers, for instance, the circular flower (red) and the half-circle (green), exhibit a larger Raman intensity than the structures with mainly upstanding walls (brown, the upper part of pink). It is important to note in this context that the size of our diffraction-limited excitation spot (500 nm, see Experimental Section) is much larger than the size of an individual flower petal. For an easy comparison, the size of the excitation spot is indicated on scale in yellow in Fig. 1(a). The Raman signal of the flowers in the Raman map is "smeared out," and the area of the plain substrate is actually much larger than it seems on the Raman maps [compare Fig. 1(c) with the SEM image in Fig. 1(a)]. The reason for the "smearing out" is that we measure a convolution of the excitation and detection volume with the spatial distribution of the optical response of the flowers. It is to be expected that the spatial distribution of the optical response of the nanoflower response is related to the size of the flower features.

Figure 1(d) presents optical spectra of the WS_2 nanoflowers. The spectra contain 8–10 Raman features, where the first two features are the characteristic vibrational modes of WS_2 (see Fig. S2 in the supplementary material). The first feature is a combination of the in-plane vibrational mode E_{2g} and the longitudinal acoustic phonon 2LA(M) (in WS_2, the frequency of these modes is almost the same), and the second feature is the out-of-plane vibrational mode A_{1g}. We attribute the higher frequency Raman features to multiphonon resonances involving the LA(M) phonon, excited because the 595 nm laser is in resonance with the A-exciton, in accordance with the attribution for WS_2 pyramids[15] (see Sec. II A in the supplementary material for details).

The spectra in Fig. 1(d) are collected from different positions of the sample: on the Si_3N_4 substrate (green), on a dense nanoflower (red), and on a vertical-wall nanoflower (pink) [indicated with stars in Fig. 1(c)]. It is interesting to note that the only difference between the red spectrum of the more dense flower and the pink spectrum of the vertical-wall flower is in the overall Raman intensity and not in the spectral position of the Raman peaks. In other words, there are no specific Raman features more or less pronounced for flowers with different nanogeometries.

The WS_2 nanoflowers exhibit a strongly reduced photoluminescence (PL) with respect to horizontally layered WS_2. On some flowers, no PL can be observed from the nanoflowers within our detection efficiency. Specific parts of some nanoflowers do exhibit a low PL, which becomes apparent especially at cryogenic temperatures [see Fig. S1(d) in the supplementary material, which depicts the PL from an exfoliated trilayer and five layers of exfoliated WS_2, measured under the same conditions as the optical response of the nanoflowers]. At 4 K, the optical response of a WS_2 nanoflower is at most 2% of the PL of a monolayer WS_2. Assuming that the absorption and the effective collection efficiency remain constant, we conclude that the CVD grown WS_2 nanoflowers have a lower quantum efficiency than horizontal WS_2 flakes. Here, the assumption of constant absorption is reasonable given the petal thickness, whereas the assumption of constant effective collection efficiency is related to the unknown emission pattern from the nanoflower petals and, therefore, less strong. We attribute the decrease in the quantum efficiency to the increase in possible non-radiative loss channels due to the presence of all the edges of the nanoflower petals. This leads to severe quenching of the exciton photoluminescence, without influencing the Raman response.

B. Polarization-resolved Raman response

To investigate the optical differences between different flowers in more detail, we study the interaction of the flower Raman response with linearly polarized light. Here, we excite the WS_2 nanoflowers with linearly polarized light, rotating the polarization direction from vertical to horizontal, and analyze the resulting emission intensity [see Fig. 3(a) for a schematic of our setup, where the quarter-wave plate and the polarization analyzer are not used in the current section]. The absence of a polarization analyzer in this measurement scheme allows us to study only the material response to the polarization direction of the excitation light, separating the influence of polarized excitation from the polarization of the emission. The additional experimental advantage of collecting all the emitted Raman intensity, independent of polarization, is the higher signal.

Figure 2(a) depicts an SEM image of a flower-like WS_2 structure [indicated in brown in Fig. 1(a)] with mainly wall-like petals, oriented in the x–z plane (see the coordinate system). Figures 2(b)–2(d)

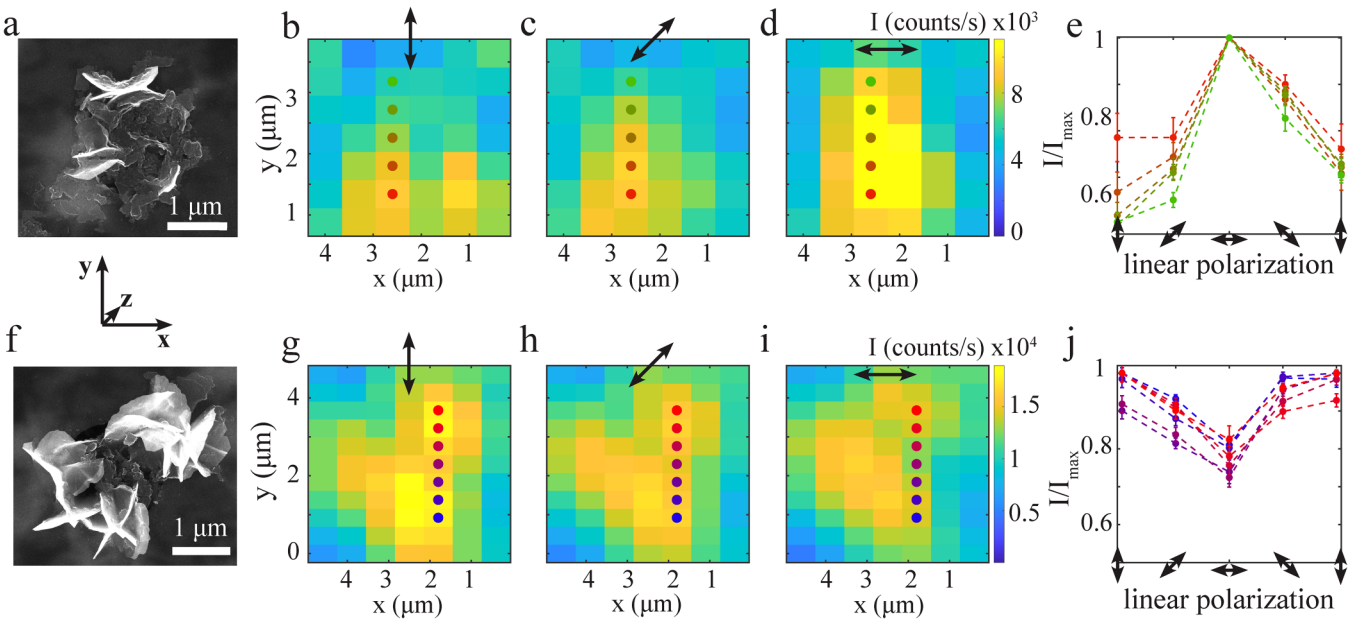

FIG. 2. Excitation polarization. (a) SEM image of a WS_2 flower-like structure [brown circle in Fig. 1(a)] with mainly petals oriented in the x–z plane. (b)–(d) and (g)–(i) Map of the intensity of the A_{1g} Raman mode of the flower-like structure upon (b) and (g) vertically polarized, (c) and (h) diagonally polarized, and (d) and (i) horizontally polarized excitation. (e) Raman intensity of the flower in (a) [used pixels are marked with full circles in (b)–(d)] as a function of excitation polarization angle, where the error bars represent the effect of a random position error in the image alignment procedure (see Sec. III B in the supplementary material). Note that the intensity increases drastically when the polarization direction is parallel to the WS_2 flower petals. (f) SEM image of a WS_2 flower [orange circle in Fig. 1(a)] with mainly petals oriented in the y–z plane. (j) Raman intensity of the flower in (f) [used pixels are marked with full circles in (g)–(i)] as a function of excitation polarization angle, where the error bars represent the effect of a random position error in the image alignment procedure (see Sec. III B in the supplementary material). Note that the intensity decreases drastically when the polarization direction is perpendicular to the WS_2 flower petals.

depict the intensity of the A_{1g} Raman mode upon vertical polarization excitation, excitation polarization at 45° and horizontal polarization excitation. The Raman intensity is the highest when the excitation polarization direction is parallel to the orientation of the nanoflower petals, in this case upon horizontal excitation [Fig. 2(d)]. Even though the diffraction-limited spotsize of the excitation light is relatively large compared to the size of the WS_2 nanoflowers, the measured Raman response exhibits a clear polarization dependence. This becomes even more apparent in Fig. 2(e), where the normalized Raman intensity of different parts of the nanoflower [positions are indicated in Figs. 2(b)–2(d)] is plotted as a function of the polarization angle (depicted by the arrows). The noise in the data is most probably caused by sub-pixel positioning imprecisions (see Sec. III B in the supplementary material). The Raman intensity upon vertical polarization is 60%–80% of the Raman intensity upon horizontal polarization. Note in Fig. 2(b) that the small flower petal to the right of the flower, oriented vertically in the y–z plane, can only be distinguished upon vertical polarization: it is not visible anymore in Figs. 2(c) and 2(d).

To illustrate the correlation between the Raman intensity of differently oriented flower-like structures and the excitation polarization even more, Fig. 2(f) depicts a nanoflower [indicated in orange in Fig. 1(a)], which exhibits petals oriented in the y–z plane (see the coordinate system). Here, the Raman intensity upon vertical y polarization excitation [Fig. 2(g)] is higher than upon horizontal x polarization excitation [Fig. 2(i)]. Figure 2(j) depicts the normalized Raman intensity of different parts of the nanoflower [positions are indicated in Figs. 2(g)–2(i)] as a function of polarization angle (depicted by the arrows). For this flower, the Raman intensity upon horizontal excitation is now 70%–90% of the Raman intensity upon horizontal polarization. The lower contrast can be explained by the angular distribution of the petal of this nanoflower. This nanoflower also contains petals oriented differently from strictly in the y–z plane, which demonstrates the sensitivity of this method. Flowers with petals oriented in random different directions do not exhibit polarization dependence (see Fig. S4 in the supplementary material).

The response of Raman modes to polarized light is described by Raman polarizability tensors based on the crystal symmetries in the material.[20,33–35] It is interesting to point out that the measured E_{2g} and A_{1g} Raman features exhibit the same polarization response (see Fig. S5 in the supplementary material). This indicates that the Raman polarization tensor for both the in-plane (E_{2g}) and the out-of-plane (A_{1g}) Raman modes are the same. We also found that the polarization dependence of the Raman intensity does not depend on temperature and is also observed upon 561 nm excitation (see Fig. S5 in the supplementary material). We conclude that linear-polarization-resolved Raman measurements provide a way to distinguish between differently oriented WS_2 petals and to identify the dominant orientation.

C. Helicity of Raman features

Another tool to investigate potential optical differences between nanoflowers with diverse geometries is helicity-resolved Raman measurements. Figure 3(a) depicts a schematic representation of our setup. The excitation light (595 nm wavelength) passes through a quarter-wave plate and is focused on the sample through an objective lens (see Experimental Section for details on the setup). The emission is collected through the same objective lens, passes a quarter-wave plate, and is directed to a spectrometer through a polarization analyzer. This allows the detection of the polarization state of the emitted light; i.e., it allows for helicity-resolved measurements. Figures 3(b) and 3(c) depict helicity-resolved nanoflower spectra. Here, the flowers are excited with σ_+ circularly polarized light, and the helicity of the Raman features is determined from the difference in σ_+ and σ_- emission. In Fig. 3(b), the blue spectrum with the same polarization as the excitation light has a higher intensity (σ_+, helicity is conserved) than the red spectrum with the opposite polarization (σ_-, helicity is reversed). We calculate the helicity of the A_{1g} Raman mode $H = \frac{I_{conserved} - I_{reversed}}{I_{conserved} + I_{reversed}}$ to be 0.138. In Fig. 3(c), the helicity-reversed spectrum (red) has a higher intensity than the helicity-conserved spectrum (blue), with $H = -0.10$.

The helicity of the Raman response of the WS_2 nanoflowers is position dependent. Figure 3(d) presents a map of the nanoflower intensity of the A_{1g} Raman mode [compare Fig. 1(c)]. Figure 3(e) presents a map of the experimentally determined helicity of the A_{1g} Raman mode [stars indicate the position of spectra in

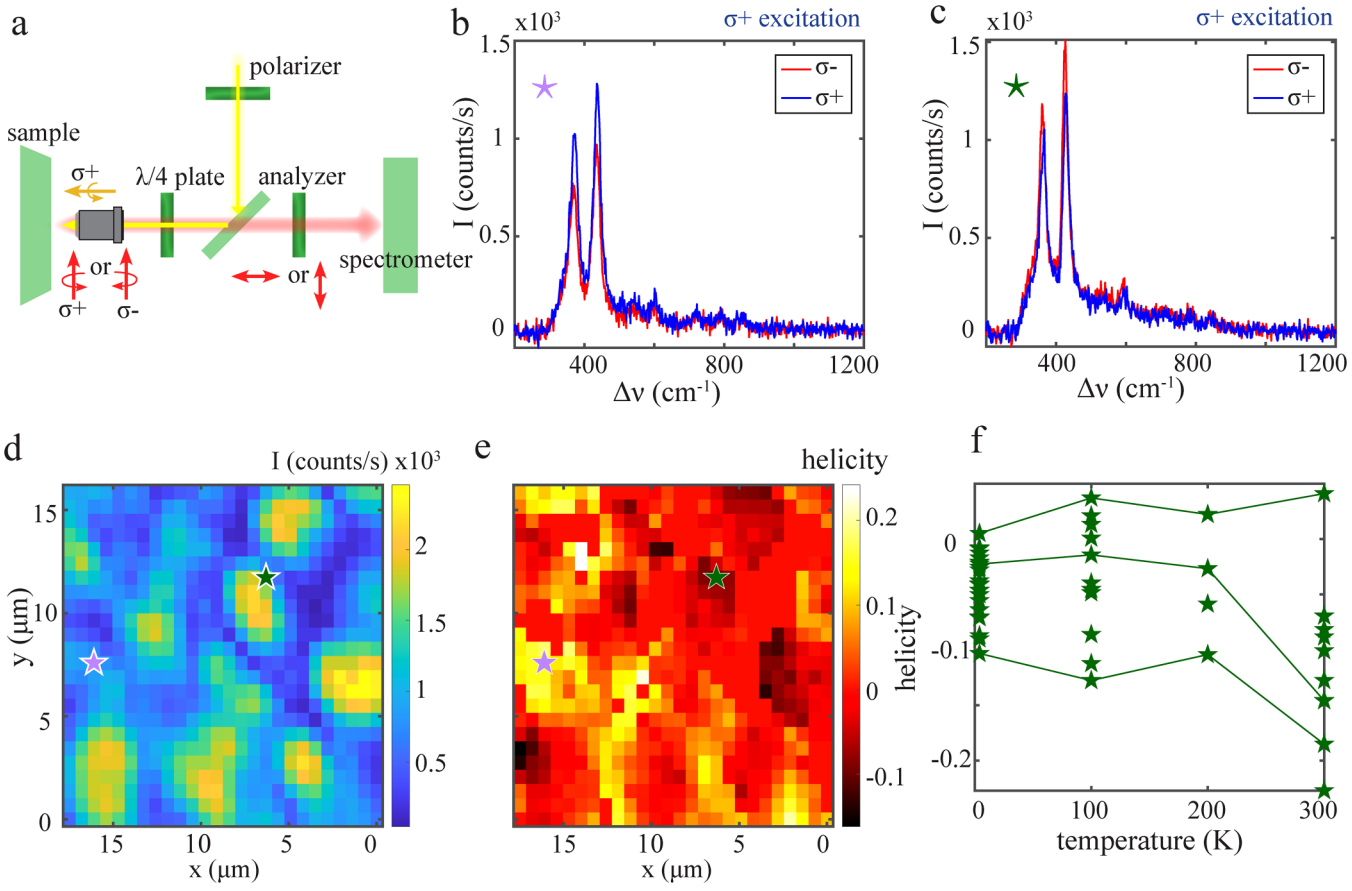

FIG. 3. Helicity of Raman features. (a) Schematic of our setup, where the excitation light (595 nm wavelength) passes through a quarter-wave plate and is focused on the sample. The emission is collected in epi-configuration and passes through the same quarter-wave plate. Then, it is directed to a spectrometer through a polarization analyzer. (b) and (c) Helicity-resolved nanoflower spectra, where the flowers are excited with σ_+ light, and the helicity is determined from the difference in σ_+ and σ_- emission. In (b), the spectrum with the same polarization as the excitation light (blue) has a higher intensity (helicity is conserved). In (c), the spectrum with opposite polarization to the excitation light (red) has a higher intensity (helicity is reversed). (d) Map of the intensity of the A_{1g} Raman mode of the nanoflower spectra. (e) Map of the same region of the helicity of the A_{1g} Raman mode. Note that the helicity of the Raman features around the WS_2 nanoflowers is negative (green star), whereas the Raman helicity is positive in regions next to the larger nanoflowers (lilac star). (f) Temperature-dependent helicity of the WS_2 nanoflower marked in green in Fig. 1(a) (taking into account all pixels associated with this flower). The lines present the temperature dependence of three locations on the flower marked in green [see Figs. S6(a) and S6(b) in the supplementary material for the taken pixels]. The overall helicity decreases slightly at room temperature.

Figs. 3(b) and 3(c)]. Note again that the measured position-dependent Raman intensity and helicity are a convolution of the excitation and detection volume with the spatial distribution of the optical response of the flowers related to the size of the flower features. This convolution does not prevent the observation of structure dependence of the Raman helicity. The Raman helicity of the WS_2 nanoflowers is negative: the intensity is higher for the helicity-reversed spectrum. Note, however, that the locations where the most negative Raman helicity is located are not in the middle of the nanoflower but toward the edge [e.g., compare the green star in Figs. 3(e) and 3(d)]. We, therefore, conclude that we detect the negative Raman helicity at locations where the excitation spot interacts with the side of a nanoflower. The helicity is most positive on locations in between the WS_2 nanoflowers, for instance, at the position of the lilac star: here, the intensity is higher for the helicity-conserved spectrum. The Raman response from these regions confirms the presence of WS_2; e.g., this is not the bare substrate. Comparing the position of the lilac star in Fig. 3(d) with the SEM image in Fig. 1(a), it seems that the region of positive helicity is actually related to the WS_2 structure to the left of the flower indicated in orange in Fig. 1(a). As this structure looks more flat than the wall-like petals in other flowers, we conclude that the sign of the Raman helicity becomes positive when the WS_2 is oriented in the x–y plane, horizontally with respect to the surface [see Fig. 1(b) for a coordinate system].

The Raman helicity response of the WS_2 nanoflowers is completely different from that of flat layers of WS_2. As alluded to before, the WS_2 nanoflowers exhibit a crystallographic 2H/3R polytypism, whereas naturally occurring WS_2 is crystallized in the 2H phase. The response of Raman modes to polarized light is described by Raman tensors[31,33,34] (see Sec. V in the supplementary material). Since the Raman tensor of the A_{1g} mode has the same symmetrical shape for 2H-WS_2 and 3R-WS_2[36] (see Sec. V in the supplementary material), it is reasonable to assume that the shape of the Raman tensor is the same for the WS_2 nanoflowers with a crystallographic 2H/3R polytypism. For all TMD materials, the Raman tensor dictates that the A_{1g} mode is helicity-conserved.[30,31] This means that the second Raman feature in Figs. 3(b) and 3(c) should only have had contributions with the same polarization as the excitation (σ_+), leading to $H = 1.0$. However, we observe a large contribution of light with the reversed helicity; in Fig. 3(c), the helicity even becomes negative in places.

Interpreting the helicity behavior of the first Raman feature is less straightforward, as this feature contains both the 2LA(M) phonon and the E_{2g}, and the Raman tensor of the E_{2g} is different for the 2H and 3R polytypes (see Fig. S6 in the supplementary material for a helicity map of the E_{2g} mode). Moreover, for the 2H polytype, the Raman tensor depends on the resonance of the excitation. The tensor dictates that the E_{2g} mode is helicity-reversed under non-resonant excitation[30] and helicity-conserved under resonant excitation of 2H-WS_2.[31,32] It is reasonable to assume that the resonance of the excitation will also influence the Raman tensor of 3R-WS_2 and 2H/3R polytypical WS_2, making the calculation of the correct tensor a non-arbitrary task. Therefore, we will focus our discussion on the Raman response of the A_{1g} mode.

It is important to note that the Raman polarization tensors are typically defined with respect to the crystal axes of flat TMDs layers, which for flat layers are readily connected to a suitable frame of reference of the incident light. The petals of the WS_2 nanoflowers exhibit a variety of orientations with respect to the incident light. Mathematically, a change of WS_2 flake orientation corresponds to a base transformation changing the Raman tensor, which may lead to allowed modes becoming forbidden and forbidden modes becoming allowed (see Fig. S8 in the supplementary material). From Fig. 3(e), it is apparent that the Raman helicity of the WS_2 nanoflowers is, in general, slightly negative, with a larger helicity-reversed than helicity-conserved contribution. This corresponds to the nanoflowers on average having more wall-like petals [oriented in the x–z or y–z plane, see Fig. 1(b) for a coordinate system], which is in agreement with the SEM images of the flowers. However, the fact that the helicity is at most -0.2, the contribution of both flat and vertically oriented flower petals within the diffraction-limited excitation spot is relatively large, and the measured Raman helicity is almost averaged out.

Based on the Raman tensor, flat flower petals (oriented in the x–y plane) should exhibit positive helicity (see Sec. V in the supplementary material). Comparing the helicity map with the SEM image in Fig. 1(a), it is not always straightforward to correlate the regions of positive helicity with the orientation and nanogeometry of flower petals. We hypothesize that there might be flat flakes present that cannot be clearly distinguished from the Si_3N_4 substrate, but that do contribute to the positive Raman helicity. We conclude that the surprising helicity values for the nanoflower Raman response can be explained by the different orientations of the flower petals.

We determine the position-dependent helicity of the Raman features at different temperatures (see Fig. S7 in the supplementary material). Figure 3(f) depicts the temperature dependence of the Raman helicity of the flower marked in green in Figs. 1(a) and 1(c). At all temperatures, the intensity is depicted of the A_{1g} Raman mode of all spectra associated with this flower. The lines present the temperature dependence of three specific places on the flower marked in green [see Figs. S6(a) and S6(b) in the supplementary material]. The helicity at room temperature seems to be slightly lower than the helicity at cryogenic temperatures, but the trend is not clear. The helicity of the first Raman feature and of the A_{1g} mode of spectra of other flowers also decreases at room temperature [see Figs. S6(d) and S6(e) in the supplementary material]. The lower helicity at room temperature can be explained by the excitation energy being more out-of-resonance with the excitonic bandgap energy (see Fig. 4). We conclude that the main mechanism that determines the Raman helicity is the flower petal orientation and, therefore, independent of temperature. Therefore, helicity-dependent Raman spectroscopy can be readily used to determine the orientation of WS_2 flakes and the contribution of flat vs wall-like petals in WS_2 nanoflowers.

D. Temperature-dependent Raman spectroscopy

Given the phononic nature of Raman scattering, studying the temperature dependence of the Raman spectra of the WS_2 nanoflowers provides valuable information. Figures 4(a) and 4(b) present the spectral response of the flower indicated in red in Fig. 1(a) (see Fig. S4 in the supplementary material for an SEM image) upon

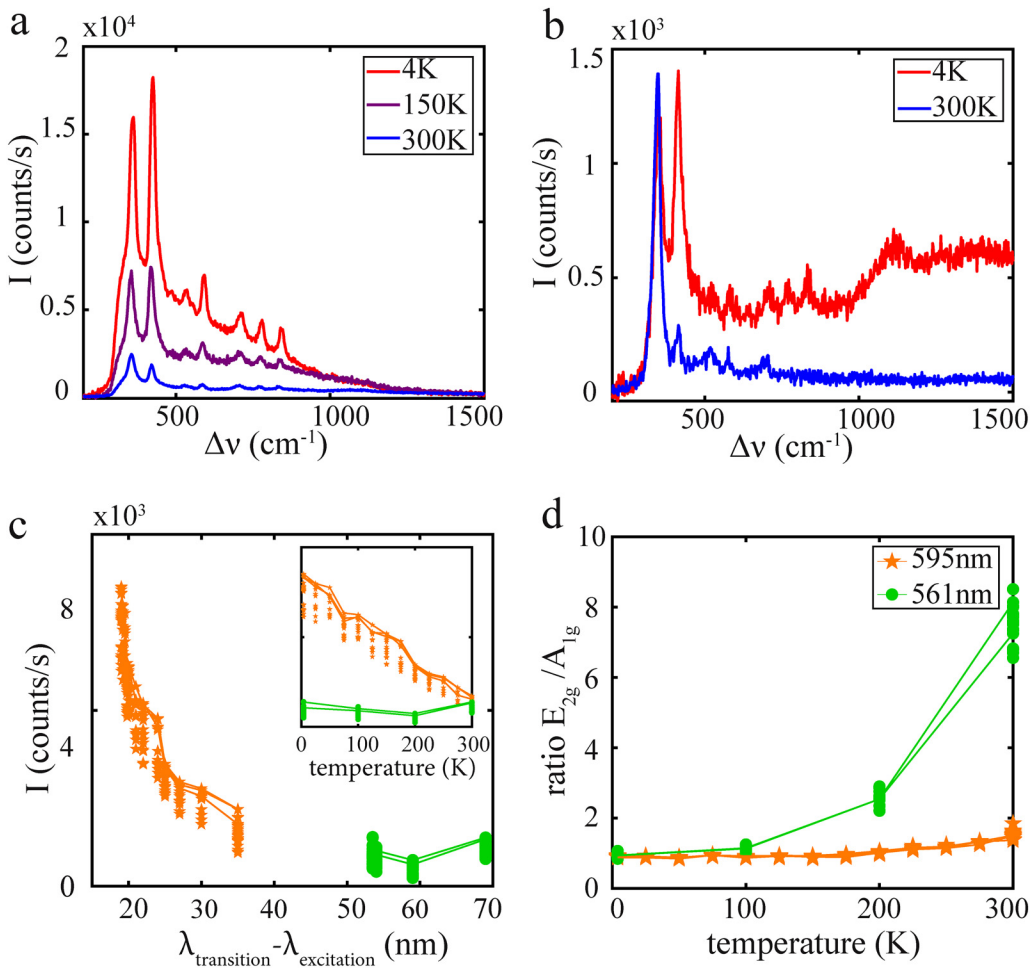

FIG. 4. Temperature dependence Raman intensity. (a) Nanoflower spectra [flower indicated in red in Fig. 1(a)] upon a 595 nm excitation at temperatures ranging from room temperature down to 4 K. Note that the intensity of all Raman features increases. (b) Nanoflower spectra [flower indicated in red in Fig. 1(a)] upon 561 nm excitation at room temperature and 4 K. Note that the A_{1g} mode is almost absent at room temperature. (c) (inset) Temperature-dependent intensity of the first Raman feature [E_{2g},2LA(M)] of the nanoflower spectra upon 595 nm excitation (orange) and 561 nm excitation (green). Here, at every temperature, the intensity is taken from all pixels associated with the flower [indicated in red in Fig. 1(d)]. (main) The Raman intensity is plotted as a function of the wavelength difference between the WS_2 bandgap and the excitation. Upon cooling down, the WS_2 bandgap energy blue shifts. With constant excitation energy, the difference between excitation and WS_2 bandgap energy will become smaller at lower temperatures, bringing the excitation more in resonance with the excitonic transition. (d) Temperature-dependent ratio of the first two Raman features of the nanoflower spectra. Upon 595 nm excitation, the ratio changes from 0.8 at 4 K to 1.6 at room temperature, as can already be seen by comparing the intensity of the first two Raman features in (a). Upon 561 nm excitation, the A_{1g} is almost absent at room temperature. Therefore, the ratio between the two WS_2 flower Raman features increases drastically from 1.0 at 4 K to 7.5 at room temperature.

595 nm and 561 nm excitation at different temperatures. There are 8–10 Raman features distinguishable at room temperature and at cryogenic temperatures (see Fig. S2 in the supplementary material), but the intensity of the features increases drastically with decreasing temperature. At 4 K, there is a broad background visible under the Raman features [at 200–700 cm^{-1} in Fig. 4(a) and at 1200–1500 cm^{-2} in Fig. 4(b)]. We attribute this background to highly reduced WS_2 photoluminescence (see Sec. II A in the supplementary material). The intensity of the Raman features is much lower for the 561 nm excitation than for the 595 nm excitation. This is attributed to the fact that the 595 nm excitation light is close to the A-exciton resonance of WS_2, whereas the 561 nm one is out-of-resonance with the A-exciton. Raman modes of TMDs can be greatly enhanced when they are excited in resonance with an excitonic transition.[22,23,25,26] The inset of Fig. 4(c) depicts the temperature-dependent intensity of the first Raman feature (E_{2g},2LA(M)) upon 595 nm excitation (orange) and 561 nm excitation (green). Here, for every temperature, the Raman intensity of all the spectra associated with the nanoflower is taken [flower indicated in red in Fig. 1(c)]. The lines present

the temperature dependence of three specific places on the flower. For an excitation at 595 nm, the Raman intensity decreases with increasing temperature, but for an excitation at 561 nm, the Raman intensity is independent of temperature. Figure 4(c) depicts the intensity of the first Raman feature as a function of the difference between the WS_2 exciton and the excitation wavelength. The WS_2 bandgap energy and, therefore, the exciton energy are temperature dependent, experiencing a blue shift with decreasing temperature [see Fig. S1(f) in the supplementary material for the temperature dependence of the exciton PL]. Therefore, varying the temperature of the WS_2 nanoflowers enables the tuning of the exciton resonance condition for a fixed excitation frequency. Since the exciton energy is experiencing a blue shift with decreasing temperatures, cooling down the WS_2 nanostructures will bring the excitation more in resonance with the excitonic transition. It is clear in Fig. 4(c) that the Raman intensity exhibits a resonant-like enhancement as the excitation wavelength approaches the excitonic transition. Since the 561 nm excitation is relatively far away from the WS_2 bandgap, the resonance effect on the Raman intensity upon cool down is much less visible.

When comparing the spectra upon 595 nm excitation in Fig. 4(a), it becomes apparent that the ratio between the two characteristic WS_2 Raman features (E_{2g}/A_{1g}) is temperature dependent. At room temperature, the E_{2g} mode is 1.5 times as intense as the A_{1g} mode, and at 4 K, the A_{1g} mode is 1.5 times as intense as the E_{2g} mode. It has been reported before that the different TMD Raman modes respond differently to the excitonic resonance.[25,26,37] When comparing the nanoflower spectra upon 561 nm excitation in Fig. 4(b), the low intensity of the second Raman feature (A_{1g}) at room temperature draws immediate attention. Figure 4(d) depicts the temperature dependence of the E_{2g}/A_{1g} ratio. At room temperature, the ratio between the characteristic WS_2 Raman features is around 7.0 for an excitation at 561 nm. From Fig. 4(d), we deduce that the A_{1g} Raman feature is more sensitive to the resonance conditions than the E_{2g},2LA(M) feature. Even if the 561 nm excitation is relatively far away from the exciton wavelength, the A_{1g} Raman mode is enhanced greatly at cryogenic temperatures, as the excitation is closer to the excitonic resonance. Therefore, we conclude that the absence of photoluminescence does not prevent an indirect study of the exciton, the presence of which is revealed by resonant Raman spectroscopy.

III. CONCLUSION

We have studied the optical response of CVD grown WS_2 nanoflowers. In contrast to flat WS_2 flakes, the nanoflowers exhibit a highly reduced photoluminescence enabling the study of their clear Raman response. Even though the WS_2 exciton emission is reduced in the nanoflowers, the presence of the excitons is still notable in the Raman response upon resonance excitation. We study the temperature-dependent Raman intensity and observe an enhancement for cryogenic temperatures, where the intensity of the out-of-plane Raman mode A_{1g} is enhanced more than the intensity of the in-plane Raman mode E_{2g}. We conclude that, due to the temperature-dependent bandgap and, thus, the exciton energy shift, the WS_2 nanoflowers are excited more in resonance with the excitonic transition at cryogenic temperatures, leading to a resonant effect on the Raman intensity.

Furthermore, we study the interplay between flower geometry and a spectral response. Even though the WS_2 nanoflowers have completely different geometries; at first sight, the only spectral differences between them seem to be the Raman intensity. However, helicity-resolved and polarization-resolved Raman spectroscopy reveals underlying structural and geometrical differences between flowers. Studying the Raman response upon excitation with circularly polarized light reveals completely different behavior of the Raman helicity of the flowers with respect to flat WS_2 flakes. The Raman helicity of nanoflowers with many vertical walls is slightly negative, and the Raman response of flat lying WS_2 flower petals is slightly positive. We attribute the differences between the nanoflowers and the flat WS_2 to a difference in the Raman polarization tensor, induced by the differently oriented flower petals. Studying the Raman response upon excitation with linearly polarized light, we observe that we can selectively address nanoflower petals oriented parallel to used polarization. We conclude that there is an interplay between the orientation of the flower petals, the atomic vibrational modes, and the polarization direction of the excitation light.

Therefore, we envision that temperature-dependent Raman spectroscopy will open the way to study excitonic resonance effects, and polarization-resolved Raman spectroscopy will open the way to determine the nanogeometry and orientation of WS_2 flakes.

IV. EXPERIMENTAL SECTION

The WS_2 nanoflowers are directly grown on a microchip using chemical vapor deposition (CVD) techniques. The sample preparation method is described in Ref. 19. The optical measurements are performed using a home-built spectroscopy setup, depicted schematically in Fig. 3(a). The sample is placed on a piezo stage in a Montana Cryostation S100. Measurements are performed at a range of temperatures between room temperature and 4 K. The sample is illuminated through an 0.85 NA Zeiss 100× objective. Measurements are performed using a continuous wave laser with a wavelength of 595 nm and a power of 1.6 mW/mm^2 (Coherent OBIS LS 594-60), and the excitation light is filtered out using color filters (Semrock NF03-594E-25 and FF01-593/LP-25). For the measurements depicted in Fig. 4, a continuous wave laser with a wavelength of 561 nm and a power of 3.6 mW/mm^2 is used (Cobolt 08-01/561). To avoid the depolarization consequences of tight focusing on (circular) polarization, a 2 mm laser diameter is used, slightly underfilling the objective in the excitation path. Polarizers (Thorlabs LPVIS100-MP2) and superachromatic waveplates are used to rotate linear polarization (Thorlabs SAHWP05M-700) and create circular polarization (Thorlabs SAQWP05M-700), respectively. The sample emission is collected in reflection through the same objective as in excitation and projected onto a CCD camera (Princeton Instruments ProEM 1024BX3) and spectrometer (Princeton Instruments SP2358) via a 4f lens system.

SUPPLEMENTARY MATERIAL

See the supplementary material that includes a comparison of spectra of flowers and monolayer and few-layer WS_2 flakes; an

overview of the measured Raman features; polarization-resolved Raman intensity at different flowers, temperatures, and upon different excitation energies; helicity-resolved Raman spectra of different modes and at different temperatures; and a derivation of the Raman helicity of horizontal vs vertical WS_2 flakes.

ACKNOWLEDGMENTS

M.C. acknowledges the financial support of the Kavli Institute of Nanoscience Delft through the KIND fellowship program. S.C.-B. and S.E.v.H. acknowledge funding from the ERC Starting Grant "TESLA" (No. 805021).

AUTHOR DECLARATIONS

Conflict of Interest

The authors have no conflicts to disclose.

Author Contributions

Irina Komen: Data curation (equal); Formal analysis (equal); Investigation (equal); Methodology (equal); Validation (equal); Visualization (equal); Writing – original draft (equal); Writing – review & editing (equal). **Sabrya E. van Heijst:** Data curation (equal); Resources (lead); Visualization (equal); Writing – review & editing (supporting). **Martin Caldarola:** Conceptualization (lead); Formal analysis (supporting); Investigation (supporting); Methodology (supporting); Validation (supporting); Writing – review & editing (supporting). **Sonia Conesa-Boj:** Conceptualization (supporting); Formal analysis (supporting); Methodology (supporting); Resources (supporting); Supervision (equal); Writing – review & editing (supporting). **L. Kuipers:** Conceptualization (equal); Formal analysis (equal); Investigation (equal); Methodology (equal); Supervision (equal); Validation (equal); Writing – review & editing (equal).

DATA AVAILABILITY

The data that support the findings of this study are openly available in 4TU.ResearchData at http://doi.org/10.4121/16628488.

REFERENCES

[1]K. Fai Mak, C. Lee, J. Hone, J. Shan, and T. F. Heinz, "Atomically thin MoS_2: A new direct-gap semiconductor," Phys. Rev. Lett. **105**(13), 136805 (2010).
[2]Y. J. Zhang, T. Oka, R. Suzuki, J. T. Ye, and Y. Iwasa, "Electrically switchable chiral light-emitting transistor," Science **344**(6185), 725–728 (2014).
[3]Q. Hua Wang, K. Kalantar-Zadeh, A. Kis, J. N. Coleman, and M. S. Strano, "Electronics and optoelectronics of two-dimensional transition metal dichalcogenides," Nat. Nanotechnol. **7**, 699 (2012).
[4]A. Chernikov, T. C. Berkelbach, H. M. Hill, A. Rigosi, Y. Li, O. Burak Aslan, D. R. Reichman, M. S. Hybertsen, and T. F. Heinz, "Exciton binding energy and nonhydrogenic Rydberg series in monolayer WS_2," Phys. Rev. Lett. **113**, 076802 (2014).
[5]T. Cao, G. Wang, W. Han, H. Ye, C. Zhu, J. Shi, Q. Niu, P. Tan, E. Wang, B. Liu, and J. Feng, "Valley-selective circular dichroism of monolayer molybdenum disulphide," Nat. Commun. **3**, 887 (2012).
[6]X. Xu, W. Yao, D. Xiao, and T. F. Heinz, "Spin and pseudospins in layered transition metal dichalcogenides," Nat. Phys. **10**, 343 (2014).
[7]B. Zhu, H. Zeng, J. Dai, Z. Gong, and X. Cui, "Anomalously robust valley polarization and valley coherence in bilayer WS_2," Proc. Natl. Acad. Sci. U.S.A. **111**(32), 11606–11611 (2014).
[8]J.-G. Song, J. Park, W. Lee, T. Choi, H. Jung, C. Wan Lee, S.-H. Hwang, J. Min Myoung, J.-H. Jung, S.-H. Kim, C. Lansalot-Matras, and H. Kim, "Layer-controlled, wafer-scale, and conformal synthesis of tungsten disulfide nanosheets using atomic layer deposition," ACS Nano **7**(12), 11333–11340 (2013).
[9]Y. Zhang, Y. Zhang, Q. Ji, J. Ju, H. Yuan, J. Shi, T. Gao, D. Ma, M. Liu, Y. Chen, X. Song, H. Y. Hwang, Y. Cui, and Z. Liu, "Controlled growth of high-quality monolayer WS_2 layers on sapphire and imaging its grain boundary," ACS Nano **7**(10), 8963–8971 (2013).
[10]C. Cong, J. Shang, X. Wu, B. Cao, N. Peimyoo, C. Qiu, L. Sun, and T. Yu, "Synthesis and optical properties of large-area single-crystalline 2D semiconductor WS_2 monolayer from chemical vapor deposition," Adv. Opt. Mater. **2**(2), 131–136 (2014).
[11]C. M. Orofeo, S. Suzuki, Y. Sekine, and H. Hibino, "Scalable synthesis of layer-controlled WS_2 and MoS_2 sheets by sulfurization of thin metal films," Appl. Phys. Lett. **105**(8), 083112 (2014).
[12]A. Thangaraja, S. M. Shinde, G. Kalita, and M. Tanemura, "Effect of WO_3 precursor and sulfurization process on WS_2 crystals growth by atmospheric pressure CVD," Mater. Lett. **156**, 156–160 (2015).
[13]P. Liu, T. Luo, J. Xing, H. Xu, H. Hao, H. Liu, and J. Dong, "Large-area WS_2 film with big single domains grown by chemical vapor deposition," Nanoscale Res. Lett. **12**(1), 558 (2017).
[14]Y. Jung, J. Shen, Y. Liu, J. M. Woods, Y. Sun, and J. J. Cha, "Metal seed layer thickness-induced transition from vertical to horizontal growth of MoS_2 and WS_2," Nano Lett. **14**(12), 6842–6849 (2014).
[15]I. Komen, S. E. van Heijst, S. Conesa-Boj, and L. Kuipers, "Morphology-induced spectral modification of self-assembled WS_2 pyramids," Nanoscale Adv. **3**(22), 6427–6437 (2021).
[16]Y. B. Li, Y. Bando, and D. Golberg, "MoS_2 nanoflowers and their field-emission properties," Appl. Phys. Lett. **82**(12), 1962–1964 (2003).
[17]X.-L. Li, J.-P. Ge, and Y.-D. Li, "Atmospheric pressure chemical vapor deposition: An alternative route to large-scale MoS_2 and WS_2 inorganic fullerene-like nanostructures and nanoflowers," Chem. Eur. J. **10**(23), 6163–6171 (2004).
[18]A. Prabakaran, F. Dillon, J. Melbourne, L. Jones, R. J. Nicholls, P. Holdway, J. Britton, A. A. Koos, A. Crossley, P. D. Nellist, and N. Grobert, "WS_2 2D nanosheets in 3D nanoflowers," Chem. Commun. **50**, 12360–12362 (2014).
[19]S. E. van Heijst, M. Mukai, E. Okunishi, H. Hashiguchi, L. I. Roest, L. Maduro, J. Rojo, and S. Conesa-Boj, "Illuminating the electronic properties of WS_2 polytypism with electron microscopy," Ann. Phys. **533**, 2000499 (2021).
[20]X. Fu, J. Qian, X. Qiao, P. Tan, and Z. Peng, "Nonlinear saturable absorption of vertically stood WS_2 nanoplates," Opt. Lett. **39**(22), 6450–6453 (2014).
[21]C. Lee, H. Yan, L. E. Brus, T. F. Heinz, J. Hone, and S. Ryu, "Anomalous lattice vibrations of single- and few-layer MoS_2," ACS Nano **4**(5), 2695–2700 (2010).
[22]W. Zhao, Z. Ghorannevis, K. Kumar Amara, J. Ren Pang, M. Toh, X. Zhang, C. Kloc, P. Heng Tan, and G. Eda, "Lattice dynamics in mono- and few-layer sheets of WS_2 and WSe_2," Nanoscale **5**, 9677–9683 (2013).
[23]A. Berkdemir, H. R. Gutiérrez, A. R. Botello-Méndez, N. Perea-López, A. Laura Elías, C.-I. Chia, B. Wang, V. H. Crespi, F. López-Urías, J.-C. Charlier, H. Terrones, and M. Terrones, "Identification of individual and few layers of WS_2 using Raman spectroscopy," Sci. Rep. **3**(1), 1755 (2013).
[24]M. R. Molas, K. Nogajewski, M. Potemski, and A. Babiński, "Raman scattering excitation spectroscopy of monolayer WS_2," Sci. Rep. **7**(28698679), 5036 (2017).
[25]L. P. McDonnell, C.-C. Huang, Q. Cui, D. W. Hewak, and D. C. Smith, "Probing excitons, trions, and dark excitons in monolayer WS_2 using resonance Raman spectroscopy," Nano Lett. **18**(2), 1428–1434 (2018).
[26]E. del Corro, A. Botello-Méndez, Y. Gillet, A. L. Elias, H. Terrones, S. Feng, C. Fantini, D. Rhodes, N. Pradhan, L. Balicas, X. Gonze, J.-C. Charlier, M. Terrones, and M. A. Pimenta, "Atypical exciton–phonon interactions in WS_2

and WSe_2 monolayers revealed by resonance Raman spectroscopy," Nano Lett. **16**(4), 2363–2368 (2016).
[27]K. Gołasa, M. Grzeszczyk, P. Leszczyński, C. Faugeras, A. A. L. Nicolet, A. Wysmołek, M. Potemski, and A. Babiński, "Multiphonon resonant Raman scattering in MoS_2," Appl. Phys. Lett. **104**(9), 092106 (2014).
[28]J.-H. Fan, P. Gao, A.-M. Zhang, B.-R. Zhu, H.-L. Zeng, X.-D. Cui, R. He, and Q.-M. Zhang, "Resonance Raman scattering in bulk 2H-MX_2 (M = Mo, W; X = S, Se) and monolayer MoS_2," J. Appl. Phys. **115**(5), 053527 (2014).
[29]A. P. S. Gaur, S. Sahoo, J. F. Scott, and R. S. Katiyar, "Electron-phonon interaction and double-resonance Raman studies in monolayer WS_2," J. Phys. Chem. C **119**(9), 5146–5151 (2015).
[30]S.-Y. Chen, C. Zheng, M. S. Fuhrer, and J. Yan, "Helicity-resolved Raman scattering of MoS_2, $MoSe_2$, WS_2, and WSe_2 atomic layers," Nano Lett. **15**(4), 2526–2532 (2015).
[31]Y. Zhao, S. Zhang, Y. Shi, Y. Zhang, R. Saito, J. Zhang, and L. Tong, "Characterization of excitonic nature in Raman spectra using circularly polarized light," ACS Nano **14**(8), 10527–10535 (2020).
[32]S. G. Drapcho, J. Kim, X. Hong, C. Jin, S. Shi, S. Tongay, J. Wu, and F. Wang, "Apparent breakdown of Raman selection rule at valley exciton resonances in monolayer MoS_2," Phys. Rev. B **95**, 165417 (2017).
[33]M. Jin, W. Zheng, Y. Ding, Y. Zhu, W. Wang, and F. Huang, "Raman tensor of van der Waals $MoSe_2$," J. Phys. Chem. Lett. **11**(11), 4311–4316 (2020).
[34]Y. Ding, W. Zheng, M. Jin, Y. Zhu, R. Zhu, Z. Lin, and F. Huang, "Raman tensor of layered MoS_2," Opt. Lett. **45**(6), 1313–1316 (2020).
[35]M. Hulman, M. Sojková, K. Végsö, N. Mrkyvkova, J. Hagara, P. Hutár, P. Kotrusz, J. Hudec, K. Tokár, E. Majkova, and P. Siffalovic, "Polarized Raman reveals alignment of few-layer MoS_2 films," J. Phys. Chem. C **123**(48), 29468–29475 (2019).
[36]M. I. Aroyo, A. Kirov, C. Capillas, J. M. Perez-Mato, and H. Wondratschek, "Bilbao crystallographic server. II. Representations of crystallographic point groups and space groups," Acta Crystallogr. Sect. A **62**(2), 115–128 (2006).
[37]B. R. Carvalho, L. M. Malard, J. M. Alves, C. Fantini, and M. A. Pimenta, "Symmetry-dependent exciton-phonon coupling in 2D and bulk MoS_2 observed by resonance Raman scattering," Phys. Rev. Lett. **114**, 136403 (2015).